

A novel method for the synthesis of MOF-199 for Sensing and Photocatalytic Applications

Deepika Garg

Punjabi University

Heena Rekhi

Punjabi University

Harpreet Kaur

Punjabi University

Karam Jeet Singh

Punjabi University

Ashok Kumar Malik (✉ malik_chem2002@yahoo.co.uk)

Punjabi University <https://orcid.org/0000-0003-1045-6848>

Research Article

Keywords: Cu (II)-MOF, Morphology, Crystallography, Nitroaromatic Compounds, Fluorescence Sensing, Photocatalysis, Density Functional Theory, Photoinduced Electron Transfer, Resonance Energy Transfer

Posted Date: October 22nd, 2021

DOI: <https://doi.org/10.21203/rs.3.rs-920803/v1>

License:   This work is licensed under a Creative Commons Attribution 4.0 International License.

[Read Full License](#)

Version of Record: A version of this preprint was published at Journal of Fluorescence on March 26th, 2022. See the published version at <https://doi.org/10.1007/s10895-022-02902-9>.

Abstract

Multifunctional Cu (II)-based Metal Organic Framework (MOF) [Cu₃(BTC)₂] has been synthesized by a facile electrochemical method. Crystallographic and morphological characterizations of synthesized MOF have been done using Powder X-ray Diffractometer and Scanning Electron Microscope (SEM), respectively, whereas Fourier Transform Infrared Spectroscopy (FT-IR), Energy Dispersive X-ray Spectroscopy (EDS), UV-Vis Absorption Spectroscopy and Energy Resolved Luminescence Spectroscopic studies have been used for the detailed qualitative, quantitative as well as optical analyses. Sharp PXRD peaks indicate the formation of highly crystalline MOF with face centered cubic (fcc) structure. Flakes (average length = 0.71 μm and width = 0.10 μm) and rods (average aspect ratio = ((0.1:8.3) μm) like morphologies have been observed in SEM micrographs. The presence of C, O and Cu has been confirmed by EDS analysis. Photocatalytic activity potential of the synthesized MOF has been tested using methylene blue dye (MB) as a test contaminant in aqueous media under sunlight irradiation. Selective and sensitive fluorescent sensing of different Nitroaromatic compounds (NACs) like 4-Nitroaniline (4-NA), 2-Nitroaniline (2-NA), 3-Nitroaniline (3-NA), 4-Nitrotoulene (4-NT), 2,4-Dinitrotoulene (2,4-DNT), 1,3-Dinitrobenzene (1,3-DNB), 2,6-Dinitrotoulene (2,6-DNT) has been done by exploring the photoluminescent behaviour of chemically stable Cu₃(BTC)₂. Synthesized MOF is extremely sensitive towards 4-NA, which is having PL quenching efficiency of 82.61% with highest quenching rate till reported. Indeed, a large quenching coefficient $K_{SV} = 34.02 \times 10^{-7} \text{ M}^{-1}$ and correlation coefficient $R^2 = 0.9962$ in K_{SV} plot have been elucidated with limit of detection (LOD) = 0.7544 ppb. The possible ways of luminescence quenching are successfully explained by the combination of Photoinduced Electron Transfer (PET) and Resonance Energy Transfer (RET) mechanisms. Additionally, the Density Functional Theory (DFT) calculations have been employed to support the experimental results. Cu₃(BTC)₂ fully demonstrates the power of a multi component MOF, which provides a feasible pathway for the design of novel material towards fast responding luminescence sensing and photocatalytic degradation of pollutants.

1. Introduction

Urbanization and economic development result in the problems due to extensive use of nitroaromatic compounds (NACs), toxic gases, heavy metal ions and pollutants. Security-terrorism and crime scene investigations are the areas of special concern dependent on explosive detection. Increase in the incidences of terrorist bomb attacks and overuse of land mines have become an alarming threat to human life [1]. Consequently, for the security of human life, these NACs must be detected without any delay with the simple possible methods. There are various technologies available for their detection like gas chromatography-mass spectrometry (GC-MS), liquid chromatography-mass spectrometry (LC-MS), energy dispersive X-ray spectroscopy (EDS), surface enhanced Raman spectroscopy (SERS), high-performance liquid chromatography (HPLC), electron capture detection (ECD), proton transfer reaction mass spectrometry (PTR-MS), nuclear quadrupole resonance (NQR), neutron activation analysis (NAA) and ion mobility spectrometry [2–4], but all these techniques are highly sensitive, expensive and require highly sophisticated instrumentation with further need of some special type of training [3]. Hence, these

techniques cannot be utilized for on-site field testing. Instead, fluorescence-quenching-based chemical detection proved to be a simple, sensitive, rapid and less expensive method for the quick detection of nitroaromatic compounds. It needs a fluorescent material with simple mechanism of detection via transmission of the signal in the form of charge between sensing material and the analyte [2]. Detection of nitroaromatic compounds, heavy metal ions, toxic gases and pollutants, are the major areas covered recently by chemical sensors based on porous MOFs. Nitroaromatic compounds are causing problems for human health and environment, among NACs 4-nitroaniline (4-NA) causes serious problems not only to aquatic organisms, but also to human health due to its accumulation in waste water. 4-NA is widely used as precursor in chemical synthesis of dyes, pesticides, poultry medicines, fuel additives, antiseptic agents, and important corrosion inhibitors [5]. It proves to be lethal for human health by causing various serious problems to human health including diarrhea, liver injury, skin eczema, respiratory arrest, methemoglobinemia, and anemia [6]. Due to its high persistence, biodegradability and chemical stability, it can cause long term environment damage [6]. Many developed and developing countries levied restriction on its production, usage and disposal and added it into the list of major pollutants [5]. Really, there is a need to establish rapid, selective and sensitive method for the detection of 4-NA. Currently, fluorescence sensing has been utilized on a large scale in chemistry, biology and environmental science [7–9]. Affordability, stability, quick response, simplicity, easy operation and availability of fluorescent sensors has created an interest among researchers to work in this field.

High sensitivity and low limit of detection (LOD) are the major concerns of an explosive sensor with additional high selectivity to avoid false signals. The vital class of explosives include nitroaromatic compounds. These materials have very low vapour pressure making them suitable for attachment on the high surface energy surfaces such as metals and metal oxides as compared to polymers, plastics etc. Moreover, the interaction between analyte and sensor material gets enhanced by increasing surface to volume ratio, quantum size effects and porosity [3]. Fluorescence sensors work on the principle of luminescence quenching or augmentation caused by the interaction between analyte and sensing material. This alteration in luminescence is caused due to the following reasons: (a) Crystal structure damage, (b) Exchange of cations between central cation of sensor and the targeted cations, and (c) Interaction between the NACs and sensor, which results in adsorption competition and resonance energy transfer [10].

Many industries like textile, plastic, leather and cosmetics consume large amount of water and produce coloured effluents. More than 700000 hazardous dyes from various industries are directly discharged into water bodies without any treatment, which cause serious water pollution[11]. These materials have serious environmental and human health issues due to their carcinogenic and toxic effects [12, 13]. So, as a remedy of these industrial effluents various methods have been utilized like adsorption of dyes on high surface area support, sedimentation, chemical coprecipitation, ion exchange method and use of biological membranes [14]. However, these methods are not preferred to a large extent due to their expensive equipments, time consuming processes and conversion of main pollutant into secondary pollutants, which needs further removal. Biochemical and physiochemical methods are not suitable for decolourisation of dyes from industries due to their inflexibility towards chemical oxidation and

photocatalytic stability. Moreover, researchers are also interested to utilize MOFs for the purpose of water purification and remediation of water through their potential photocatalytic activity for the degradation of dyes in water.

Therefore, there is a need of such materials, which can act both photocatalyst as well as sensor for detection of nitroaromatic compounds. The advanced oxidation process and moderate reaction conditions make Metal Organic Frameworks (MOFs) an interesting topic of the current research. MOFs are hybrid of organic linkers with metal ions/clusters, which are interconnected to form 2D or 3D porous structures [15]. Compared to inorganic semiconductors, MOFs have open metal sites, unsaturated metal centers and catalytically active linkers as a main advantage. These are rapidly developing due to their large surface areas, rich active sites, diverse structural topologies and various potential applications, such as gas storage [16], separation [12], heterogenous catalysis [13], sensing [17], photocatalytic activity [17] and so on.

Several routes have been proposed for the synthesis of MOFs like diffusion, hydrothermal / solvothermal methods [18], which require high temperature and pressure for operation. In recent years, some faster routes like sonochemical [19], mechanochemical [20] and microwave [21] have been introduced. But these have some disadvantages like high energy consumption, complex process, requirement of advanced equipment, introduction of unwanted anions with the use of metal salts, long reaction time and difficulty in regulation [22, 23]. So, for the advancement of the field a mild and clean synthesis method for the purpose of overcoming the mentioned disadvantages is required. So, there are few reports on electrochemical synthesis which is facile and environment friendly with advantages including mild reaction conditions, simple operation and cleaning process. Moreover, metal ions are produced through anodic oxidation which avoids the problematic anions such as nitrates from metal salts. In electrochemical method size and morphology can be optimized by different factors like nature of solvent, applied current, electrolyte concentration, electrodeposition time and distance between counter electrodes [24]. Protic solvent like water (green and economic) opted as a solvent and copper metal electrodes are employed instead of costlier platinum or titanium electrodes. Electrolysis have been carried out under amperostatic conditions. In the present work, Cu (II) based MOF $[\text{Cu}_3(\text{BTC})_2]$ has been synthesized using facile electrochemical method. $\text{Cu}_3(\text{BTC})_2$ shows a hydrogen bonding, which results in its three-dimensional supramolecular framework. Synthesized MOF has been characterized by various characterization techniques such as FT-IR, Powder-XRD, SEM, EDS, UV-Vis. absorption spectroscopy and photoluminescence spectroscopy to explore their potential for NACs sensing and photocatalytic applications. To the best of our knowledge, $\text{Cu}_3(\text{BTC})_2$ has been reported first time to act as a good and efficient luminescent sensor for these particular NACs: 4-NA, 2-NA, 3-NA, 4-NT, 2,4-DNT, 1,3-DNB, 2,6-DNT with selectivity towards 4-NA showing quenching efficiency and LOD to be 82.61% and 0.7544ppb, respectively. Additionally, based on the characteristics of $\text{Cu}_3(\text{BTC})_2$, it has been utilized first time for photocatalytic activity towards degradation of MB dye as a test aqueous contaminant, which showed virtuous photocatalytic activity for green degradation of MB.

2. Materials And Methods

2.1. Materials

1,3,5-benzene tricarboxylic acid (H_3BTC), sodium chloride ($NaCl$) and methylene blue (MB) were purchased from Merck Pvt. Ltd. India. N,N' -dimethylformamide (DMF), dimethylacetamide (DMA), methanol ($MeOH$), ethanol ($EtOH$) and acetone were procured from Sigma Aldrich, India. Copper electrode strips ($6\text{cm} \times 0.5\text{cm} \times 0.05\text{cm}$) were purchased from Roto Metals, India, whereas NACs: 4-Nitroaniline (4-NA), 2-Nitroaniline (2-NA), 3-Nitroaniline (3-NA), 2,4-Dinitrotoulene (2,4-DNT), 4-Nitrotoulene (4-NT), 2,6-Dinitrotoulene (2,6-DNT) and 1,3-Dinitrobenzene (1,3-DNB) were purchased from Loba Chemie, India. All the above mentioned chemicals were of analytical reagent grade and used without further purification.

2.2. MOF Synthesis

Electrochemical deposition method has been opted for the synthesis of $Cu_3(BTC)_2$ MOF. The electrolysis reaction was carried out in undivided electrolytic cell consisting of glass vessel containing 50 mg of trimesic acid (H_3BTC) dissolved in 100 ml of distilled water with addition of 1 g of $NaCl$ as a supporting electrolyte. Two copper strips ($6\text{cm} \times 0.5\text{cm} \times 0.05\text{cm}$) with similar area thoroughly cleaned with dilute hydrochloric acid and distilled water were dipped in electrolyte. A DC power supply unit (30–50 V and 20 mA) was attached to the cathode and anode strips. The electrolysis reaction media was magnetically stirred. After 2h progress of reaction, $Cu_3(BTC)_2$ sky-blue precipitates were formed at electrodes as well as in suspension. The precipitates deposited at the electrodes were scratched with knife edge, whereas the precipitates from suspension were collected using centrifugation, subsequently washed three times with distilled water and methanol. These precipitates were dried in conventional oven at $110\text{ }^\circ\text{C}$ for 24 h. This technique is a resourceful process much better than typical solvothermal and microwave synthesis methods [25] as it is an eco-friendly technique, less time consuming as well as cost effective with simple apparatus. The schematic diagram showing synthesis of $Cu_3(BTC)_2$ is shown in Fig. 1. Scheme 1 shows the basic reaction for the synthesis of MOF-199 from BTC as organic linker and Cu^{2+} as metal ion under electrochemical conditions at room temperature with addition of supporting electrolyte ($NaCl$).

Supporting electrolyte has been changed to design different morphologies of the products.

2.3. Characterization Tools and Techniques

For the detection of functional groups, FT-IR spectra have been recorded using Bruker Tensor-27 FTIR spectrometer using KBr pellet technique in the range of $500\text{--}4000\text{ cm}^{-1}$. For crystallographic analysis X-ray diffraction patterns were recorded using XPERT PRO Powder X-ray Diffractometer [$Cu\text{ K}_\alpha$ X-ray ($\lambda = 1.5406\text{ \AA}$) with power 1800W] in 2θ range 5° to 50° keeping scanning rate and step size 0.001 s^{-1} and 0.013° , respectively. The morphological features of the synthesized material has been studied using JEOL, JSM-6510LV Scanning Electron Microscope (SEM). MOF sample was mounted on sample stub with double adhesive carbon tape followed by gold coating and analysed in SEM at a working distance of 11 mm using accelerating voltage of 15kV. For elemental analysis Oxford instrument (INCA X-act) EDS spectrometer equipped as an additional accessory to SEM was used. UV-Vis. absorption

spectrophotometer (Shimadzu UV-Vis 1600) and spectrofluorometer (Shimadzu RF-5301PC) have been opted for detailed optical analysis of synthesized MOF.

2.4. Photocatalytic Experiment

Photocatalytic reaction was performed using $\text{Cu}_3(\text{BTC})_2$ as a photocatalyst in an aqueous suspension of MB dye under the sunlight irradiation at geographical coordinates: 30.33°N and 76.38°E (Average solar power incident on surface was 400 W/m^2 for 12 h). To carry out an experiment, 1 L stock solution of dye was prepared by dissolving 5 mg of MB dye in an aqueous media. To check the photobleaching of MB dye, 500 ml of pristine dye solution was exposed to sunlight for 4.5 h followed by absorption studies. Then for the photocatalytic investigation of synthesized $\text{Cu}_3(\text{BTC})_2$ photocatalyst, one batch of aqueous suspension containing 500 ml of dye solution with 40 mg of photocatalyst was prepared followed by stirring for 1 h in dark to ensure the establishment of an adsorption-desorption equilibrium. Then, this equilibrated mixed solution was exposed to direct sunlight with continuous stirring for 4.5 h. 5 ml suspension was collected after every 30 minutes of sunlight irradiation from photocatalytic chamber followed by centrifugation. Then the collected aliquot was analysed with UV-Vis. Absorption spectrophotometer to calculate the residual dye concentration.

2.5. Fluorescence Measurements

For room temperature PL measurements, 1 mg each of the $\text{Cu}_3(\text{BTC})_2$ was dissolved in 20 ml of different solvents: N,N-dimethylformamide, dimethylacetamide, methanol, water, ethanol and acetone followed by ultrasonication for 0.5 h. Then emission spectra of the above prepared solutions were recorded immediately at excitation wavelength of 380 nm.

2.5.1. Detection of NACs

To check the luminescence sensing response of MOF-199, 100 ppb solutions of different NACs : 4-NA, 2-NA, 3-NA, 4-NT, 2,4-DNT, 1,3-DNB, 2,6-DNT were prepared separately in DMF followed by ultrasonication for 10 min. 1ml each of above prepared solutions (100 ppb) was added separately into the 100 μl emulsion of MOF in DMF followed by dilution with DMF to make the net volume 3ml and sonicated for 10 min. Then the obtained emulsion containing different NACs was immediately used to record room temperature emission spectra ($\lambda_{\text{ex}} = 380 \text{ nm}$).

For further selective sensing of 4-NA various concentrations at parts per billion [25 ppb, 30 ppb, 35 ppb, 40 ppb and 45 ppb] were prepared from the stock solution by quantitative dilution.

2.5.2. Computational Methodology

For the theoretical studies, Gauss view 5.08 was used for the preparation of input file of H_3BTC and NACs. Gaussian 09 program package software has been used for geometrical optimization and HOMO-LUMO calculations. The density functional theory (DFT) calculations have been performed with subsequent geometry optimization at B3LYP/631G level.

3. Results And Discussion

3.1. Quantitative, Qualitative, Morphological and Crystallographic Analyses

Figure 2, shows FTIR spectra of the synthesized MOF along with BTC for detailed analysis of bonding between 1,3,5-benzenetricarboxylic acid and Cu^{2+} . The band observed around 1702 cm^{-1} can be significantly assigned to stretching vibration of acidic $\text{C}=\text{O}$ present in BTC. This acidic $\text{C}=\text{O}$ start deprotonation after complexation with Cu^{2+} , which is proved by shifting of characteristic peak from 1702 cm^{-1} to 1633 cm^{-1} . From the observed shifting, it is obvious that carboxylate ion participates in complex formation. Synthesized MOF-199 is free from CuO and Cu_2O [26] during its nucleation as proved by absence of their characteristic peaks at 410 cm^{-1} , 500 cm^{-1} , 610 cm^{-1} and 615 cm^{-1} in the recorded FTIR spectra. Moreover, the representative vibration at 724 cm^{-1} may be attributed to $\text{Cu}-\text{O}$ stretching vibration, in which the oxygen atom is coordinated with Cu . Broad band observed in $2500\text{--}3300\text{ cm}^{-1}$ region in benzene tricarboxylic acid is due to $\text{O}-\text{H}$ stretching in carboxylic group, which shifts to $3100\text{--}3600\text{ cm}^{-1}$ region in the complex indicating the presence of loosely bound water molecules in $\text{Cu}_3(\text{BTC})_2$. It can be clearly seen from the recorded spectra that the symmetric COO stretches of carboxylate group can be detected in the range of $1500\text{--}1600\text{ cm}^{-1}$, which forms a complex with Cu^{2+} . This recommends that deprotonation in acidic $\text{C}=\text{O}$ has arisen. BTC linker contains benzene groups, which shows a peak around 1577 cm^{-1} due to $\text{C}-\text{C}$ skeletal vibration. Cu is substituted on benzene groups via formation of coordination bond with oxygen atom, which is evidenced by a sharp peak around 753 cm^{-1} due to $\text{Cu}-\text{O}$ stretching vibration [27].

Powder X-ray diffraction pattern recorded for electrochemically synthesized $\text{Cu}_3(\text{BTC})_2$ is shown in Fig. 3. The recorded diffraction peaks situated at 2Θ values: 6.0607° , 7.499° , 9.534° , 11.662° , 12.176° , 15.096° , 16.572° , 16.973° , 18.296° , 19.165° , 22.753° , 25.678° , and 29.673° corresponding to the Miller indices (111), (200), (220), (222), (400), (331), (422), (511), (440), (600), (731), and (751), respectively, which are in good agreement with the diffractograms reported in literature [Cambridge crystallographic information data No. 112954][28, 29] reveal the formation of face centered cubic (fcc) crystal structure. Moreover, the presence of sharp diffraction peaks in the recorded diffractogram indicate the formation of crystalline $\text{Cu}_3(\text{BTC})_2$ with uniform porosity [30]. No peak in the recorded diffractogram corresponds to CuO , Cu_2O or any other impurity phase [31], which reveals the formation of high purity $\text{Cu}_3(\text{BTC})_2$.

Figure 4 [(a) & (b)] shows the SEM micrographs recorded at magnification of $\times 20,000$ and $\times 30,000$ for the morphological analysis of synthesized MOF-199. The recorded micrographs reveal the formation of flakes (average length = $0.71\text{ }\mu\text{m}$ and width = $0.10\text{ }\mu\text{m}$) and rods (average aspect ratio = $0.1:8.3\text{ }\mu\text{m}$) like morphologies with heterogeneous size distribution. Energy dispersive X-ray spectrum recorded to determine the chemical composition and purity of electrochemically synthesized $\text{Cu}_3(\text{BTC})_2$ is shown in Fig. 5. Recorded EDS spectrum shows the peaks situated at 0.3 keV and 0.5 keV corresponding to Carbon

(C) and Oxygen (O), respectively, whereas, the peaks situated at energies 1 keV, 8 keV and 9 keV correspond to Copper (Cu). The extra peak observed at 2.2 keV corresponds to sputter coated gold, which was coated to make the sample conducting for SEM studies. Detailed analysis of the EDS spectrum of $\text{Cu}_3(\text{BTC})_2$ reveals that carbon (C), oxygen(O) and copper (Cu) have weight% (atomic%) values 31.63% (53.68%), 25.58% (32.60%) and 42.79% (13.73%), respectively. Figure 6 [(a), (b) & (c)] shows colour mapping images of carbon, oxygen and copper, respectively, which indicates the formation of good superiority MOF-199 with appropriate stoichiometric ratio of constituting elements.

3.2. Photocatalytic Performance

The photocatalytic activity of $\text{Cu}_3(\text{BTC})_2$ has been studied by selecting MB dye as a model organic contaminant in aqueous media under sunlight irradiation. Figure 7 shows the UV-Vis. absorption spectrum recorded for synthesized MOF-199. It reveals that synthesized MOF has good absorption tunability with solar spectrum. Thus, the synthesized MOF can be efficiently photoactivated with sunlight. Figure 8 shows the UV-Vis absorption spectra of pristine methylene blue dye solution with and without sunlight exposure. It can be clearly seen from the recorded spectra that only 5.85 % of MB dye has been photobleached by sunlight during 4.5 h of irradiation. The recorded absorption spectra show a major absorption peak around 667 nm, which has been used as a reference peak to observe the remanant dye concentration for different duration of irradiation in the presence of photocatalyst. Figure 9 shows the time dependent absorption spectra of MB dye degraded by $\text{Cu}_3(\text{BTC})_2$ photocatalyst for different durations of sunlight irradiation that designate the decrease in absorbance of dye with passage of time. Figure 10 depicts the dye degradation efficiency of the photocatalyst as a function of irradiation time, which shows that with increase in irradiation time the degradation efficiency increases and reaches the maximum value of 88.96 % within 4.5h. Figures 9 & 10 clearly indicate that photocatalyst can degrade the dye upto 88.96%. The degradation efficiency can be calculated using following equation

$$\epsilon = C_0 - C / C_0$$

In order to study the kinetics of photocatalytic degradation of MB dye, it has been evaluated to be first order kinetics through a Langmuir Hinshelwood kinetics model [32];

$$\ln C_0/C = Kt$$

where K is the first order rate constant (h^{-1}), t is the irradiation time (h), C_0 and C are initial and final dye concentrations. Figure 11, illustrates the photocatalytic dye degradation mechanism, which indicates that generation of photoexcited charge carriers (h^+ and e^- 's) has sole responsibility of photocatalytic activity. These photoexcited charge carriers when reaches on the surface of the photocatalyst by avoiding volume and surface recombinations, then these charge carriers on the surface of the photocatalyst participate in oxidation (e^-) and reduction (h^+) reactions, which further causes the formation of hydroxyl free radicals (OH^\bullet). These hydroxyl free radicals further degrade dye into degrade dye into small molecules like CO_2

and H₂O. Moreover, photocatalyst activated surface due to hydroxyl group results in huge quantity of visible light absorption, which results in enhancing photocatalytic activity [33].

4. Selection Of Solvent For Photoluminescence Studies

As Cu₃(BTC)₂ has a good chemical stability in numerous solvents. Thus, room temperature PL measurements of Cu₃(BTC)₂ were performed with different solvents to achieve maximum luminescence quantum yield. For the selection of appropriate solvent following solvents: DMF, DMA, methanol, ethanol and water have been investigated. Figure 12 [(a) & (b)] shows the solvent dependent PL spectra of MOF-199 dissolved in different solvents. It can be clearly seen from the recorded spectra as well as histogram, that emission intensity is extremely dependent on the type of solvent. Moreover Figure 12 [(a) & (b)] indicates that MOF-199 dissolved in DMF has strongest PL intensity, whereas the weakest PL intensity is observed in case of acetone. Thus, the DMF has been selected as an appropriate solvent to check luminescence based sensing ability of synthesized MOF-199 due to its optical analytic effect. Figure 13 shows the PL emission spectra recorded at different excitation wavelengths ranging from 380 nm to 410 nm. It can be clearly observed from recorded spectra that 380 nm is a suitable excitation wavelength, which give maximum PL intensity. After the selection of solvent and excitation wavelength, room temperature PL spectra of Cu₃(BTC)₂ and BTC were recorded for the detailed optical analysis of synthesized MOF-199. Figure 14 shows the recorded PL spectra of Cu₃(BTC)₂ and BTC alongwith excitation spectra. The emission band maxima are situated at 465 nm and 436 nm for Cu₃(BTC)₂ and BTC, respectively. Due to close proximity in emission bands, the PL of Cu₃(BTC)₂ is due to π - π^* ligand centered electronic transitions. Additionally, red shift in emission of Cu₃(BTC)₂ w.r.t. BTC is probably due to increase in ligand conformational rigidity and reduction of non-radiative decay. From the recorded spectra, it has been clearly demonstrated that there is two fold enhancement in PL intensity in the MOF compared to ligand.

4.2. Sensing of NACs

Excellent luminescence and chemical stability of Cu₃(BTC)₂, make it a potential candidate for sensing of NACs. To check the sensing ability of MOF-199 for the detection of nitroaromatic compounds (NACs), PL response experiments were performed using different NACs: 4-NA, 2-NA, 3-NA, 4-NT, 2,4-DNT, 1,3-DNB and 2,6-DNT. PL spectra (λ_{ex} = 380 nm) of NACs@MOF-199 (100ppb) shown in Figure 15 (a) reveal that the addition of analyte in phosphor solution efficiently quenches luminescence. Histogram in Figure 15(b) shows MOF-199 PL intensity variation as a function of analyte NACs. It depicts that 4-NA quenches the PL intensity to maximum extent, whereas 2,4-DNT has minimal quenching ability. For detailed analysis, PL quenching efficiency of different NACs is shown in Figure 15 (c), which indicates that 4-NA has maximum quenching efficiency of 86.12% followed by 23.64%, 19.20%, 14.13%, 11.36%, 7.52% and 2.24% for 2-NA, 4-NT, 2,6-DNT, 3-NA, 1,3-DNB, and 2,4-DNT, respectively. Due to excellent quenching efficiency of 4-NA, it was selected for further detailed sensing studies.

Thus, for sensitivity studies, concentration dependent PL quenching behaviour of 4-NA was studied by varying its concentration from 25 ppb to 45 ppb. Figure 16 (a) shows MOF-199 luminescence quenching at different concentrations of 4-NA. Kinetics of a photophysical intermolecular deactivation process can be described by Stern-Volmer relationship given below:

$$I_0/I = 1 + K_{SV}[A]$$

where I_0 and I represent luminescence intensity before and after addition of analyte, ' K_{SV} ' is Stern-Volmer constant in (M^{-1}) and ' $[A]$ ' represents concentration of analyte in ppb.

Figure 16(b) shows K_{SV} curve of MOF-199 at different concentrations of 4-NA, this linear SV plot has $R^2 = 0.9962$ and $K_{SV} = 34.02 \times 10^{-7} M^{-1}$, which reveal that emission intensity diminishes due to dynamic quenching. The limit of detection (LOD) of $Cu_3(BTC)_2$ sensor has been calculated by the following equation:

$$LOD = 3\sigma/K$$

where σ represents standard deviation and K is Stern-Volmer constant. Calculated value of LOD is observed to be as low as 0.7544 ppb for 4-NA.

Comparison of the calculated LOD value with other research reports (as shown in table 1) reveal that the synthesized MOF is an efficient sensor for the high precision detection of NACs. The detection of nitroaromatic compounds by MOFs can be described by following two mechanisms: (1) Photo-induced electron transfer (PET); (2) Resonance energy transfer (RET). To check whether the PET mechanism is operative, HOMO-LUMO energies of various NACs and BTC organic ligand have been calculated by DFT method using B3LYP/631G basis set. The LUMO of NACs are present at lower energy than conduction band edge of MOFs, which acts as a driving force to intensify excited electron transfer from electron rich MOFs to electron deficient NACs. According to Frontier Molecular Orbital (FMO) theory, lesser the gap between highest occupied molecular orbital (HOMO) to lowest unoccupied molecular orbital (LUMO), easier will be electron transitions. As evident from previous reports, the LUMO of NACs are situated between the HOMO and LUMO of MOF [34]. Thus, it is evident that transitions from HOMO of MOF can easily take place to LUMO of NACs, which results the quenching of MOFs fluorescence. Figure 17 shows HOMO and LUMO energies of electron deficient NACs and BTC. From Figure 17, it can be clearly seen that LUMO energies of different NACs follows the following order:



which are not fully in accordance with observed experimental results. Figure 18 (a) represents the structures of various Nitroaromatic Compounds (NACs), whereas Figure 18 (b) signifies the optimized structures of one unit of $Cu_3(BTC)_2$, BTC (ligand) and various nitroaromatic compounds using DFT calculations through Gaussian 09 package with subsequent geometry optimization at B3LYP/631G level to analyse the connectivity modes. Above discussed results reveal that PET is not appropriately

describing the PL sensing mechanism. So, for the detailed illustration of quenching mechanism along with PET, RET is also playing an important role.

The sensitivity and quenching efficiency can be properly explained by RET, which depends upon the extent of overlap between the emission spectrum of donor $[\text{Cu}_3(\text{BTC})_2]$ and absorption spectrum of each analyte [NACs]. Figure 19 shows the emission and absorption spectra of donor and analytes, respectively. The large spectral overlap between the absorption peak of 4-NA with emission peak of $\text{Cu}_3(\text{BTC})_2$ signifies the probability of charge carrier/energy transfer from MOF to analytes due to weak interactions between the two, thus leading to the selective quenching phenomenon. However, no such spectral overlap has been observed for other NACs as depicted in Figure 19, which explains the selectivity towards 4-NA. Thus, it is concluded that RET along with PET can thoroughly explain the fluorescence quenching mechanism. Hence, both electron transfer and energy transfer mechanisms could reasonably explain MOF-199 PL quenching by NACs [35].

Conclusions

Electrochemical method provides an efficient, low cost, eco-friendly route for the synthesis of MOF-199. Synthesized MOF crystallizes in face centred cubic (fcc) structure having flakes and rods like morphologies. Due to high chemical stability, synthesized MOF-199 acts as a good photocatalyst to degrade MB dye with degradation efficiency of 88.96%. Synthesized MOF proves to act as a good sensor for the detection of NACs with selectivity towards 4-NA with quenching coefficient (K_{SV}) and quenching efficiency values of $6.63 \times 10^5 \text{ M}^{-1}$ and 99%, respectively, alongwith 0.7544 ppb limit of detection (LOD). PET and RET are the potential mechanisms to thoroughly explain fluorescence-based sensing ability of MOFs. MOF-199 has enough capability to act as an excellent candidate for both photo-catalytic and chemical sensing applications. Rapid preparation, photocatalytic activity and efficient sensing of $[\text{Cu}_3(\text{BTC})_2]$ enable it to be a potential candidate for environment governance.

Declarations

Funding (information that explains whether and by whom the research was supported)

One of the authors, Deepika is grateful to University Grants Commission (UGC), New Delhi, India, for providing junior research fellowship. Heena, one of another authors is also thankful to the UGC, New Delhi, India, for providing financial support under College for Potential and Excellence research grant with reference number KCP/2020/MS/2174-2179.

-Conflicts of interest/Competing interests (include appropriate disclosures)

All the authors declare that there is no conflict of interest.

-Ethics approval/declarations (include appropriate approvals or waivers)

There are no ethic approvals required for this research work.

-Consent to participate (include appropriate statements)

All authors will participate in the revision of the manuscript.

-Consent for publication (include appropriate statements)

All authors agree for the publication.

-Availability of data and material/ Data availability (data transparency, if link please provide the link to access).

Data and material information is provided and will be shared on request.

-Code availability (software application or custom code)

This is not applicable.

-Authors' contributions

Deepika Garg : Performed the experimentation

Heena : Helped in performing the experiments

Harpreet Kaur Helped in performing the experiments

Karam Jeet Singh and Ashok Kumar Malik: Helped in writing and supervised the research work

Table 1 represents the various selected bond distances (Å) and angles (°) for Cu₃(BTC)₂ in optimized structure

References

1. Jiang N, Li G, Che W, Zhu D, Su Z, Bryce MR (2018) Polyurethane derivatives for highly sensitive and selective fluorescence detection of 2, 4, 6-trinitrophenol (TNP). *Journal of Materials Chemistry C* 6(42):11287–11291
2. Ding SB, Wang W, Qiu LG, Yuan YP, Peng FM, Jiang X, Zhu JF (2011) Surfactant-assisted synthesis of lanthanide metal-organic framework nanorods and their fluorescence sensing of nitroaromatic explosives. *Mater Lett* 65(9):1385–1387
3. George G, Edwards CS, Hayes JI, Yu L, Ede SR, Wen J, Luo Z (2019) A novel reversible fluorescent probe for the highly sensitive detection of nitro and peroxide organic explosives using electrospun BaWO₄ nanofibers. *Journal of Materials Chemistry C* 7(47):14949–14961

4. Håkansson K, Coorey RV, Zubarev RA, Talrose VL, Håkansson P (2000) Low-mass ions observed in plasma desorption mass spectrometry of high explosives. *Journal of mass spectrometry* 35(3):337–346
5. Zheng K, Zhang TC, Lin P, Han YH, Li HY, Ji RJ, Zhang H Y. 4-Nitroaniline degradation by TiO₂ catalyst doping with manganese. *Journal of Chemistry*, 2015
6. Xie W, Zhang J, Zeng Y, Wang H, Yang Y, Zhai Y, Li L (2020) Highly sensitive and selective detection of 4-nitroaniline in water by a novel fluorescent sensor based on molecularly imprinted poly (ionic liquid). *Anal Bioanal Chem* 412(23):5653–5661
7. Pallares RM, Sutarlie L, Thanh NT, Su X (2018) Fluorescence sensing of protein-DNA interactions using conjugated polymers and graphene oxide. *Sens Actuators B* 271:97–103
8. Han XY, Fan QX, Chen ZH, Deng LX, Fang ZQ, Shi G, Zhang M (2019) Coordination polymers of Tb³⁺/Nucleotide as smart chemical nose/tongue toward pattern-recognition-based and time-resolved fluorescence sensing. *Biosensors Bioelectronics* 139:111335
9. Meroni M, Rossini M, Guanter L, Alonso L, Rascher U, Colombo R, Moreno J (2009) Remote sensing of solar-induced chlorophyll fluorescence: Review of methods and applications. *Remote Sens Environ* 113(10):2037–2051
10. Zhan Z, Liang X, Zhang X, Jia Y, Hu, M (2019) A water-stable europium-MOF as a multifunctional luminescent sensor for some trivalent metal ions (Fe³⁺, Cr³⁺, Al³⁺), PO₄³⁻ ions, and nitroaromatic explosives. *Dalton Trans* 48(5):1786–1794
11. Mahmoodi NM, Abdi J (2019) Nanoporous metal-organic framework (MOF-199): Synthesis, characterization and photocatalytic degradation of Basic Blue 41. *Microchem J* 144:436–442
12. Bloch ED, Queen WL, Krishna R, Zadrozny JM, Brown CM, Long JR (2012) Hydrocarbon separations in a metal-organic framework with open iron (II) coordination sites. *Science* 2012335(6076):1606–1610
13. Rasero-Almansa AM, Corma A, Iglesias M, Sánchez F (2014) Design of a Bifunctional Ir–Zr Based Metal–Organic Framework Heterogeneous Catalyst for the N-Alkylation of Amines with Alcohols. *ChemCatChem* 6(6):1794–1800
14. Ahmed MA, El-Katori EE, Gharni ZH (2013) Photocatalytic degradation of methylene blue dye using Fe₂O₃/TiO₂ nanoparticles prepared by sol–gel method. *J Alloy Compd* 553:19–29
15. Goto Y, Sato H, Shinkai S, Sada K (2008) “Clickable” metal – organic framework. *J Am Chem Soc* 130(44):14354–14355
16. Farha OK, Yazaydin A, Eryazici I, Malliakas CD, Hauser BG, Kanatzidis MG, Hupp JT (2010) De novo synthesis of a metal–organic framework material featuring ultrahigh surface area and gas storage capacities. *Nature chemistry* 2(11):944–948
17. Wu Y, Wu J, Xie B, Zou L, Li Y, Han Y, Wu X (2017) Designing functional metal-organic frameworks from a new tripodal carboxylate ligand: Fluorescence sensing and photocatalytic properties. *J Lumin* 192:775–782

18. Al-Kutubi H, Gascon J, Sudhölter EJ, Rassaei L (2015) Electrosynthesis of metal–organic frameworks: challenges and opportunities. *ChemElectroChem* 2(4):462–474
19. Jung DW, Yang DA, Kim J, Kim J, Ahn WS (2010) Facile synthesis of MOF-177 by a sonochemical method using 1-methyl-2-pyrrolidinone as a solvent. *Dalton Trans* 39(11):2883–2887
20. Garay AL, Pichon A, James, S (2007) L.Solvent-free synthesis of metal complexes. *Chem Soc Rev* 36(6):846–855
21. Ni Z, Masel RI (2006) Rapid production of metal – organic frameworks via microwave-assisted solvothermal synthesis. *J Am Chem Soc* 128(38):12394–12395
22. Pirzadeh K, Ghoreyshi AA, Rahimnejad M, Mohammadi M (2018) Electrochemical synthesis, characterization and application of a microstructure Cu_3 (BTC) $_2$ metal organic framework for CO_2 and CH_4 separation. *Korean J Chem Eng* 35(4):974–983
23. Yang HM, Xian LIU, Song XL, Yang TL, Liang ZH, Fan CM (2015) In situ electrochemical synthesis of MOF-5 and its application in improving photocatalytic activity of BiOBr. *Transactions of Nonferrous Metals Society of China* 25(12):3987–3994
24. Varsha MV, Nageswaran G Direct Electrochemical Synthesis of Metal Organic Frameworks. *Journal of the Electrochemical Society*. 2020
25. Huang X, Chen Y, Lin Z, Ren X, Song Y, Xu Z, Wang B (2014) Zn-BTC MOFs with active metal sites synthesized via a structure-directing approach for highly efficient carbon conversion. *Chem Commun* 50(20):2624–2627
26. Ardelean I, Cora S, FT-IR (2008) Raman and UV–VIS spectroscopic studies of copper doped $3\text{Bi}_2\text{O}_3 \cdot \text{B}_2\text{O}_3$ glass matix. *J Mater Sci: Mater Electron* 19(6):584–588
27. Kumar RS, Kumar SS, Kulandainathan MA (2013) Efficient electrosynthesis of highly active Cu_3 (BTC) $_2$ -MOF and its catalytic application to chemical reduction. *Microporous Mesoporous Mater* 168:57–64
28. Dong J, Zhao D, Lu Y, Sun WY (2019) Photoluminescent metal–organic frameworks and their application for sensing biomolecules. *Journal of Materials Chemistry A* 7(40):22744–22767
29. Biemmi E, Christian S, Stock N, Bein T (2009) High-throughput screening of synthesis parameters in the formation of the metal-organic frameworks MOF-5 and HKUST-1. *Microporous Mesoporous Mater* 117(1–2):111–117
30. Sun B, Kayal S, Chakraborty A (2014) Study of HKUST (Copper benzene-1, 3, 5-tricarboxylate, Cu-BTC MOF)-1 metal organic frameworks for CH_4 adsorption: An experimental Investigation with GCMC (grand canonical Monte-carlo) simulation. *Energy* 76:419–427
31. Chui SSY, Lo SMF, Charmant JP, Orpen AG, Williams (1999) I. D. A chemically functionalizable nanoporous material $[\text{Cu}_3(\text{TMA})_2(\text{H}_2\text{O})_3]_n$. *Science* 283(5405):1148–1150
32. Kalered E. *Quantum chemical studies of deposition and catalytic surface reactions* (Vol. 1925) Linköping University Electronic Press. 2018

33. Yang J, Chen C, Ji H, Ma W, Zhao J (2005) Mechanism of TiO₂-assisted photocatalytic degradation of dyes under visible irradiation: photoelectrocatalytic study by TiO₂-film electrodes. *J Phys Chem B* 109(46):21900–21907
34. Lu L, He J, Wang J, Wu WP, Li B, Singh A, Qin X (2019) Luminescent sensing and photocatalytic degradation in a new 3D Zn (II)-based highly luminescent metal – organic framework. *J Mol Struct* 1179:612–617
35. Tanwar AS, Meher N, Adil LR, Iyer PK (2020) Stepwise elucidation of fluorescence based sensing mechanisms considering picric acid as a model analyte. *Analyst* 145(14):4753–4767
36. Chakraborty G, Das P, Mandal SK (2018) Strategic construction of highly stable metal–organic frameworks combining both semi-rigid tetrapodal and rigid ditopic linkers: selective and ultrafast sensing of 4-Nitroaniline in water. *ACS applied materials interfaces* 10(49):42406–42416
37. Chakraborty G, Das P, Mandal SK (2019) Structural Diversity in Luminescent MOFs Containing a Bent Electron-rich Dicarboxylate Linker and a Flexible Capping Ligand: Selective Detection of 4-Nitroaniline in Water. *Chemistry–An Asian Journal* 14(20):3712–3720

Tables

TABLE 1: Selected bond distances (Å) and angles (°) for Cu₃(BTC)₂

C(1)-C(2)	C(37)-O(39)	1.37800
C(2)-C(3)	O(39)-H(40)	0.99561
C(3)-C(4)	C(21)-C(29)	1.48014
C(4)-C(5)	C(29)-O(30)	1.22724
C(5)-C(6)	C(29)-O(31)	1.37846
C(6)-H(17)	O(31)-H(32)	0.99564
C(5)-C(13)	C(5)-C(6)-H(17)	120.81777
C(13)-O(14)	H(8)-C(4)-C(5)	119.84371
C(13)-O(15)	H(7)-C(2)-C(1)	120.61906
O(15)-H(16)	C(9)-C(1)-C(6)	117.44906
C(4)-H(8)	C(1)-C(9)-O(10)	125.39694
C(1)-C(9)	O(11)-C(9)-O(10)	123.15349
C(9)-O(10)	H(12)-O(11)-C(9)	108.76795
C(9)-O(11)	C(2)-C(3)-C(18)	119.78463
O(11)-H(12)	C(18)-C(3)-C(4)	119.98154
C(3)-C(18)	O(19)-C(18)-O(20)	116.33749
C(18)-O(19)	O(20)-Cu(41)-O(19)	70.22772
C(18)-O(20)	O(35)-Cu(41)-O(34)	70.22782
C(2)-H(7)	O(35)-C(33)-O(34)	116.33723
Cu(41)-O(19)	O(35)-C(33)-C(25)	121.86376
Cu(41)-O(20)	O(34)-C(33)-C(25)	121.71881
Cu(41)-O(34)	C(21)-C(22)-C(23)	119.60999
Cu(41)-O(35)	C(22)-C(23)-C(24)	120.52647
C(33)-O(35)	C(23)-C(24)-C(25)	119.51847
C(33)-O(34)	C(24)-C(25)-C(26)	120.23427
C(25)-C(33)	C(25)-C(26)-H(36)	120.32434
C(25)-C(26)	C(25)-C(24)-H(28)	119.86011
C(24)-C(25)	C(23)-C(22)-H(27)	119.57230
C(23)-C(24)	C(24)-C(23)-C(37)	122.02459

C(22)-C(23)	C(26)-C(21)-C(29)	117.58625
C(21)-C(22)	O(38)-C(37)-O(39)	123.15360
C(21)-C(26)	C(37)-O(39)_H(40)	108.76782
C(26)-H(36)	C(29)-O(31)-C(29)	108.71506
C(22)-H(27)	O(31)-C(29)-O(30)	123.15676
C(24)-H(28)	C(1)-C(2)-C(3)	119.5185
C(23)-C(37)	C(2)-C(3)-C(4)	120.23370
C(37)-O(38)	C(3)-C(4)-C(5)	

Table 1: Comparison with the reported MOFs

Method	LOD (ppb)	References
Zn-MOF	88 ppb	[36]
Zn(II)-MOF	0.74 ppm	[37]
Cd(II)-MOF	0.46 ppm	[37]
Cu-MOF	0.7944ppb	Present method

Figures

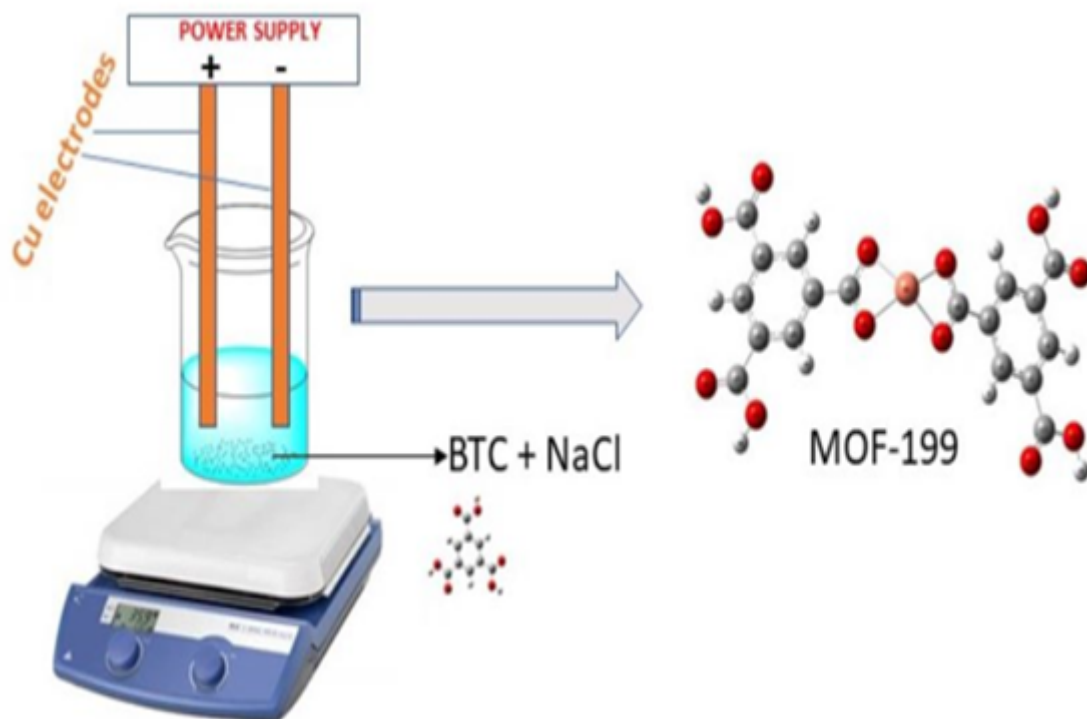


Figure 1

Schematic of MOF-199 synthesis

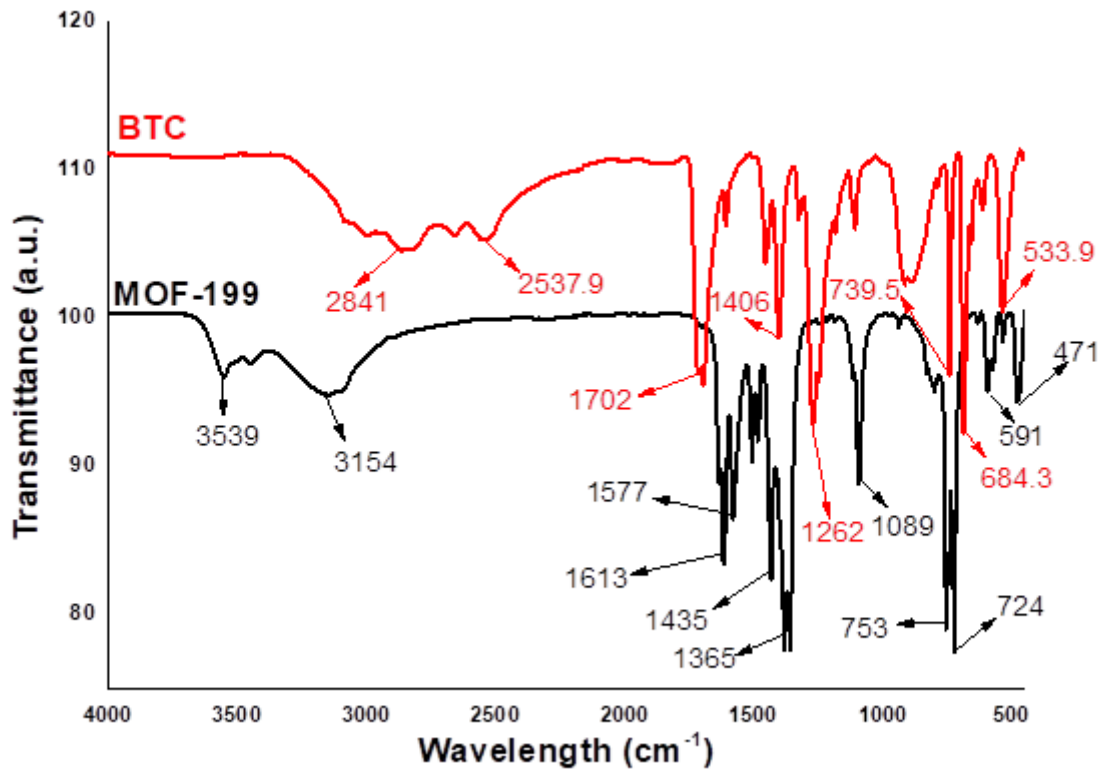


Figure 2

FTIR spectra of synthesized MOF-199 and BTC

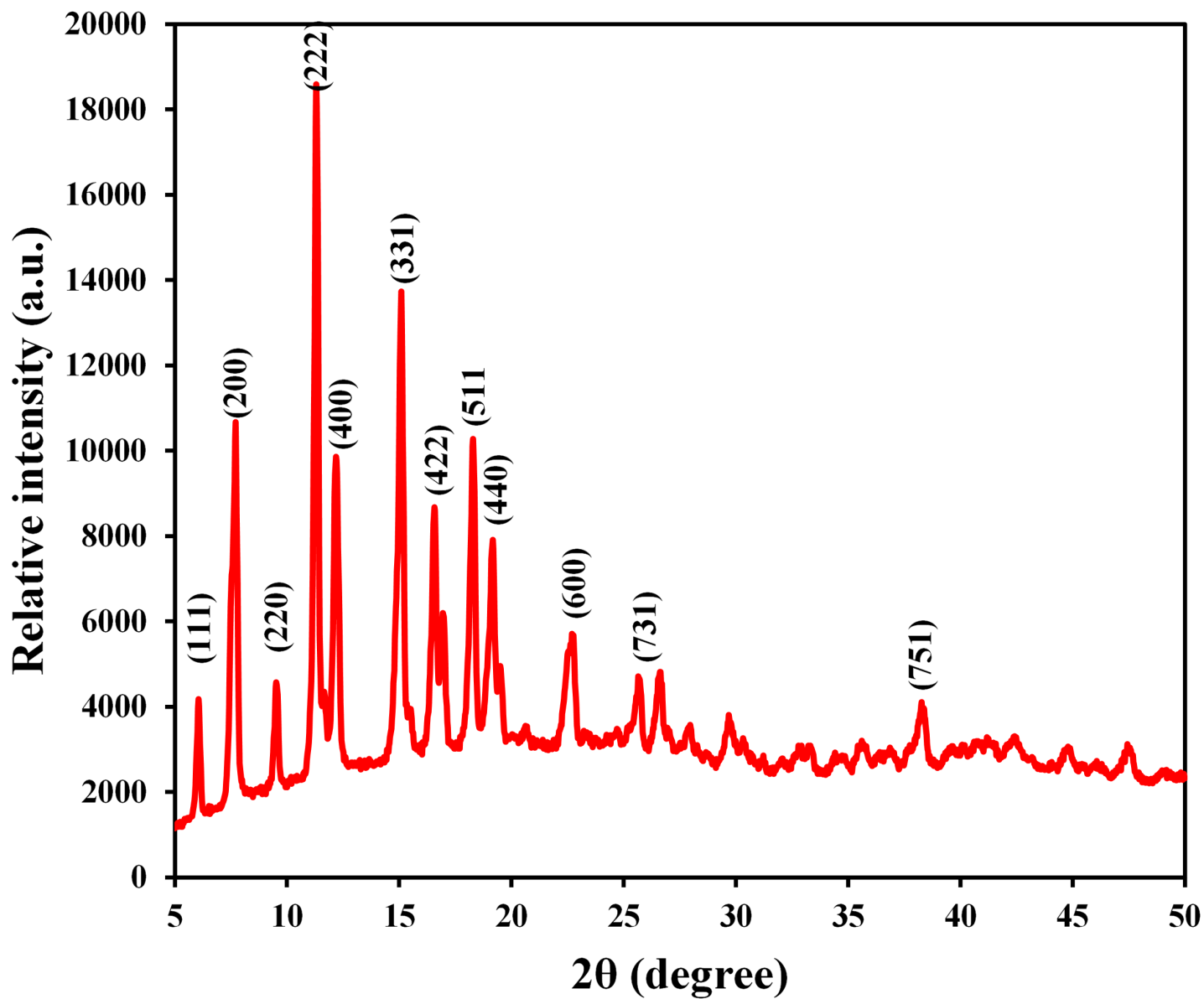


Figure 3

Powder XRD diffractogram of synthesized MOF-199

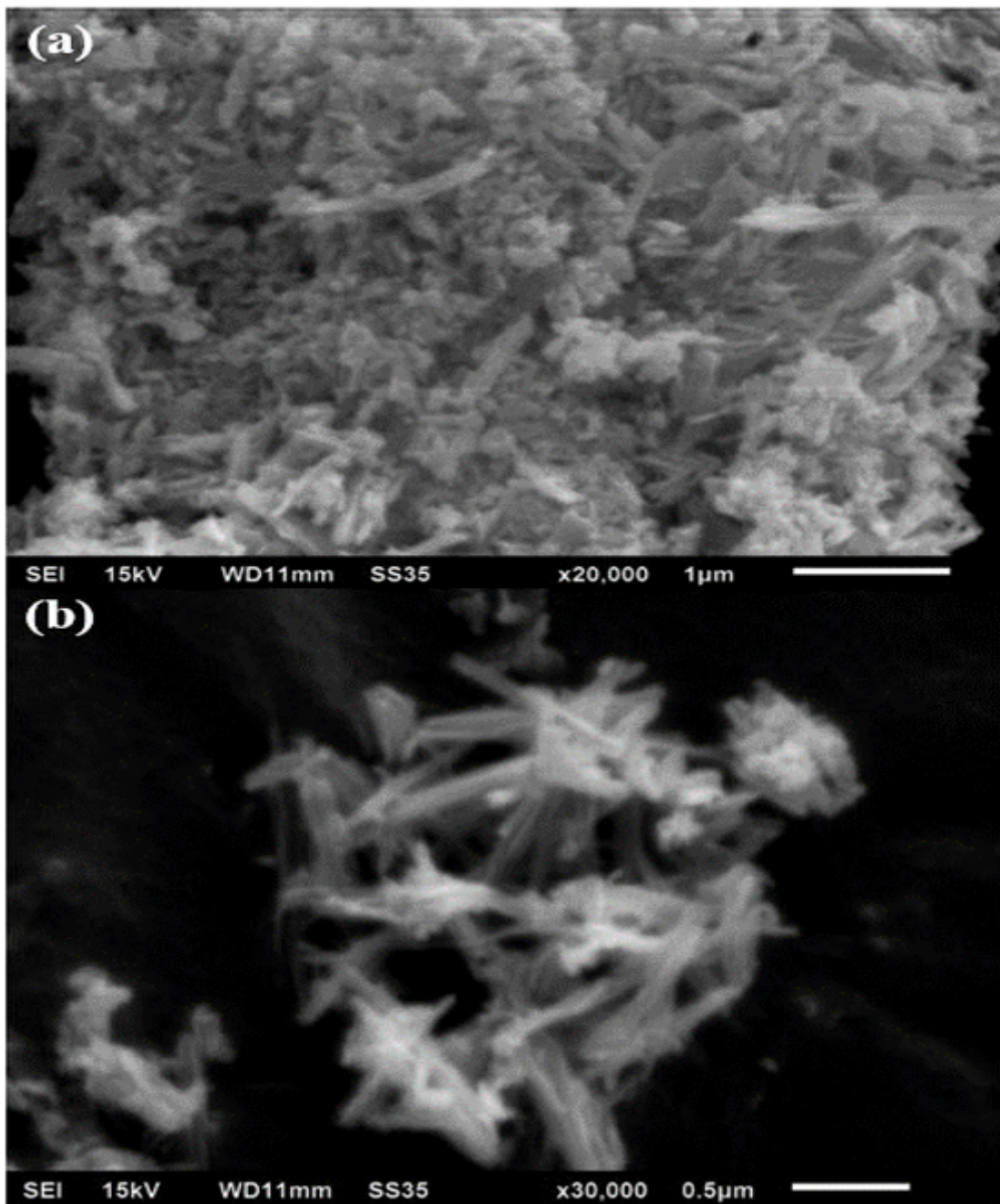


Figure 4

SEM micrographs of MOF-199 with different magnifications (a) x20,000 (b) x30,000.

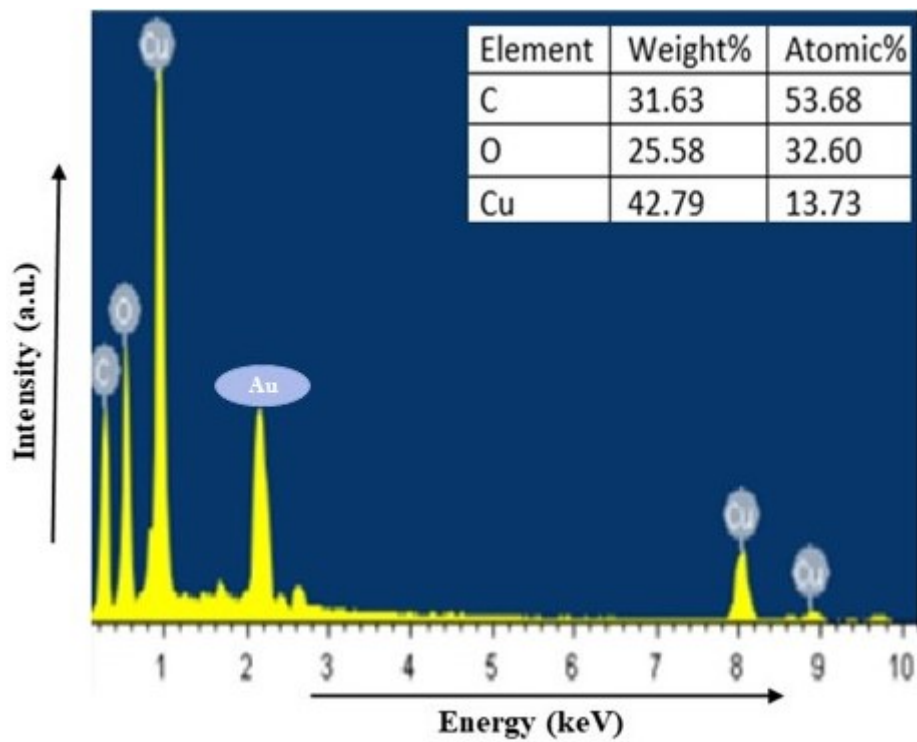


Figure 5

EDS spectra of synthesized MOF-199 sample

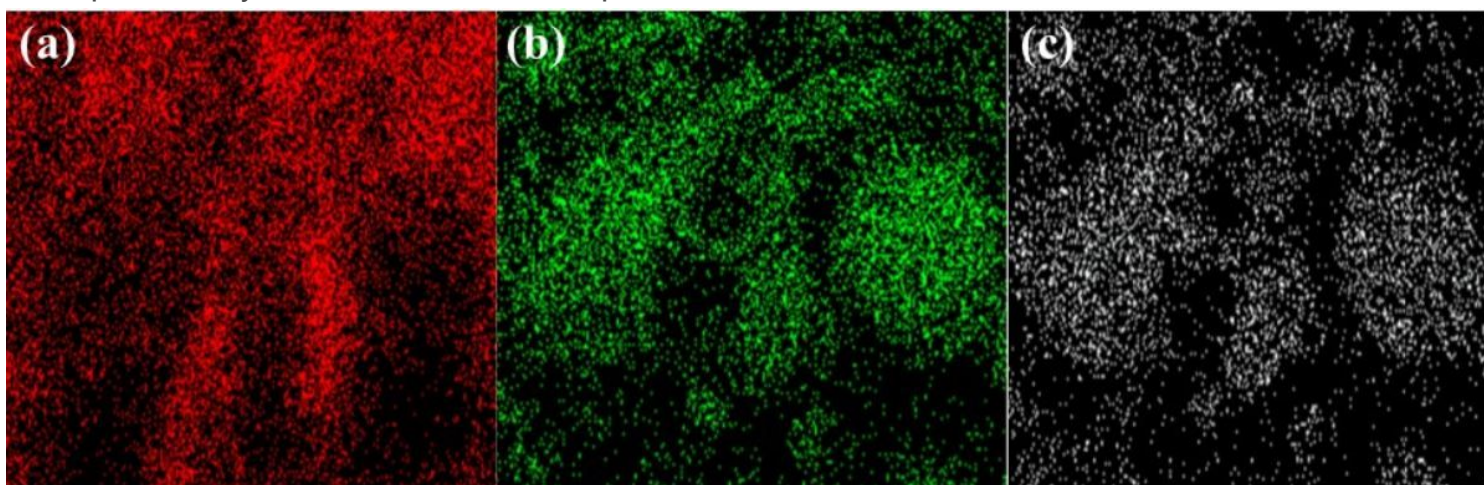


Figure 6

SEM-EDS mapping images of elements in MOF-199 (a) Carbon (C) (b) Oxygen (O) (c) Copper (Cu)

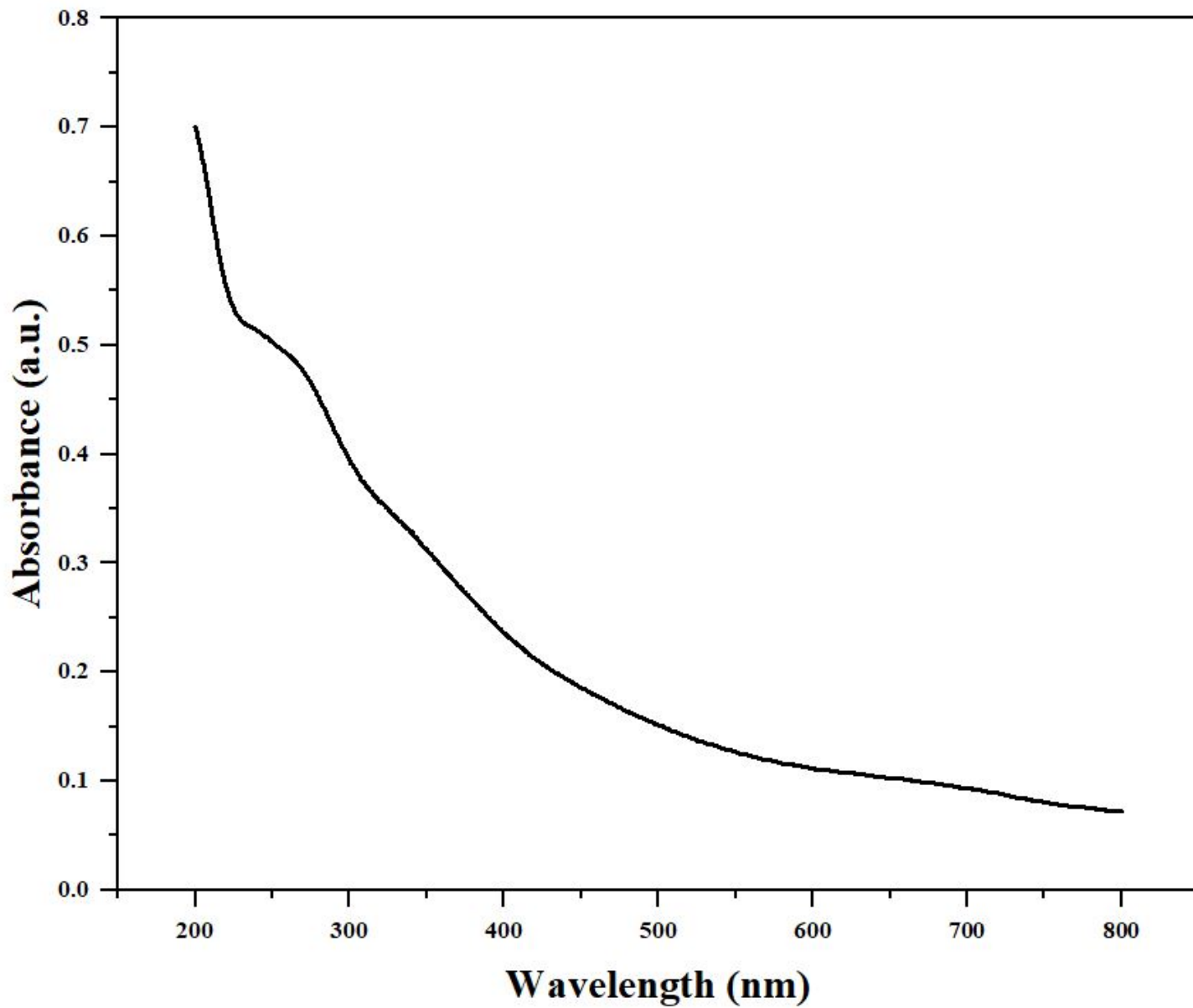


Figure 7

UV-Vis absorption spectrum of synthesized MOF-199

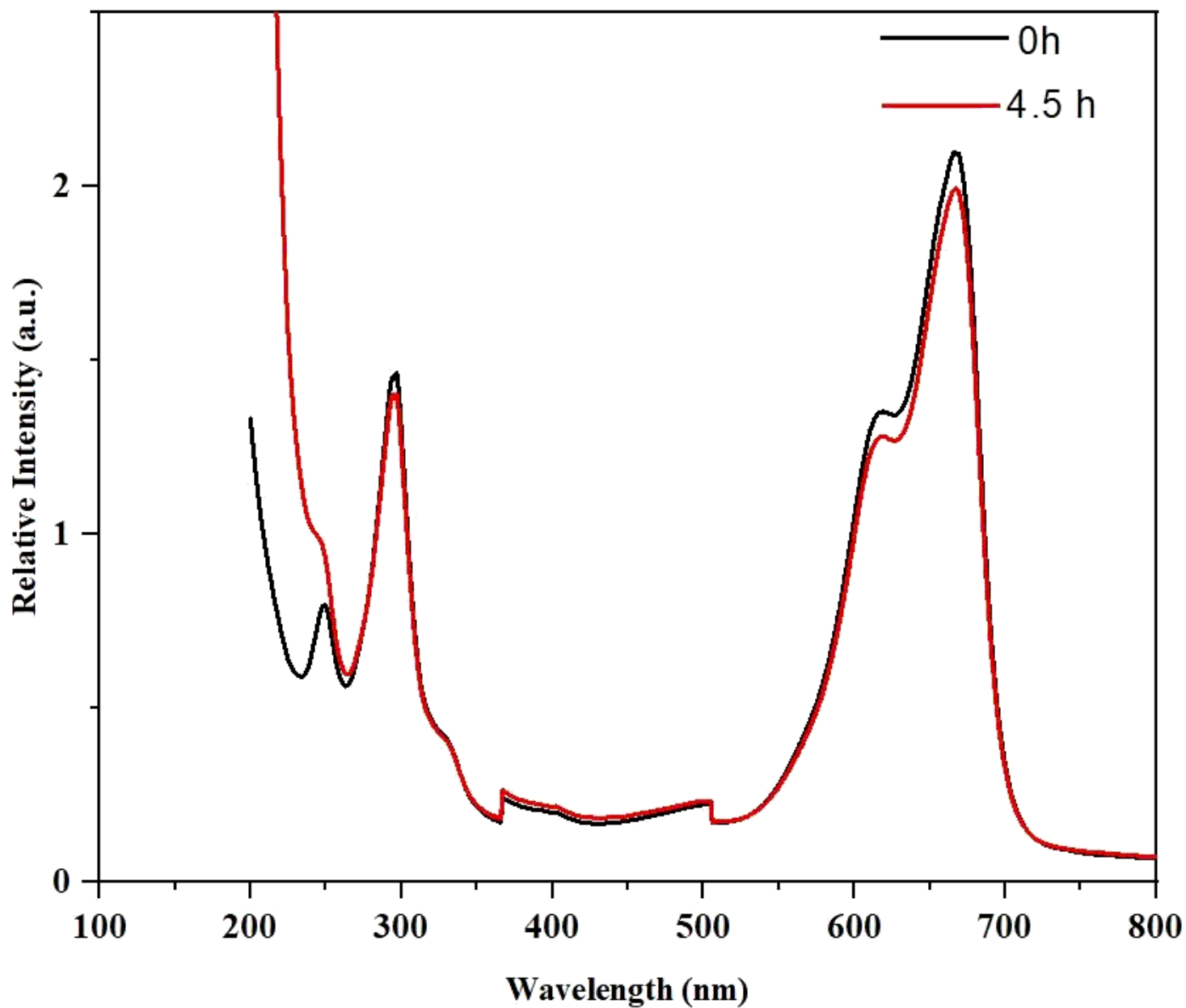


Figure 8

UV-Vis absorption spectra of aqueous methylene blue dye solution with 4.5h sunlight irradiation and without sunlight exposure

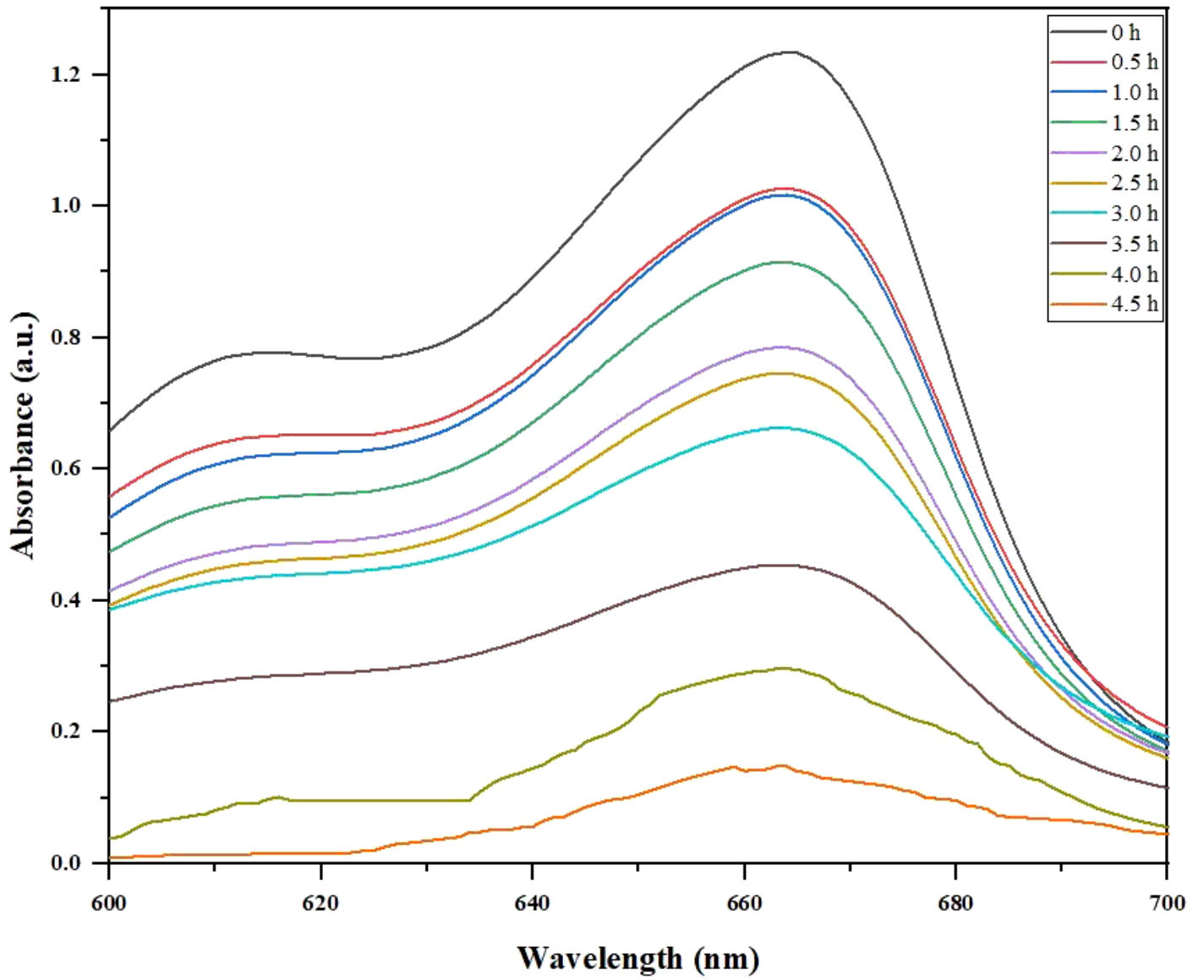


Figure 9

Time dependent absorption spectra of methylene blue dye degraded in presence of $\text{Cu}_3(\text{BTC})_2$.

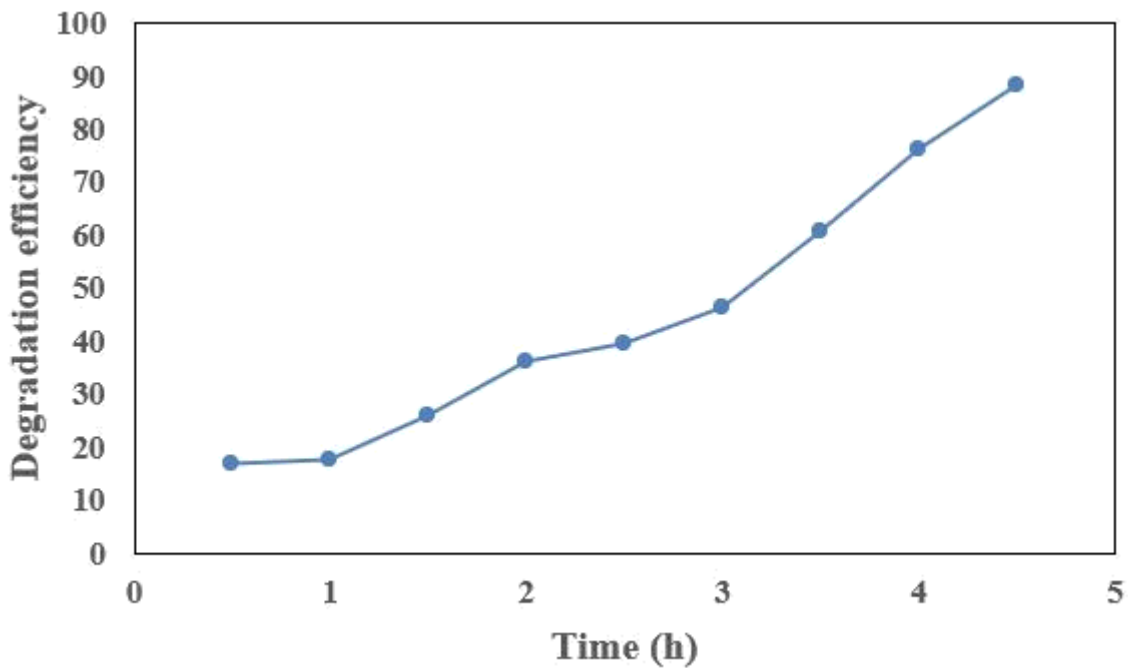


Figure 10

Degradation efficiency of $\text{Cu}_3(\text{BTC})_2$ photocatalyst for the degradation of MB dye

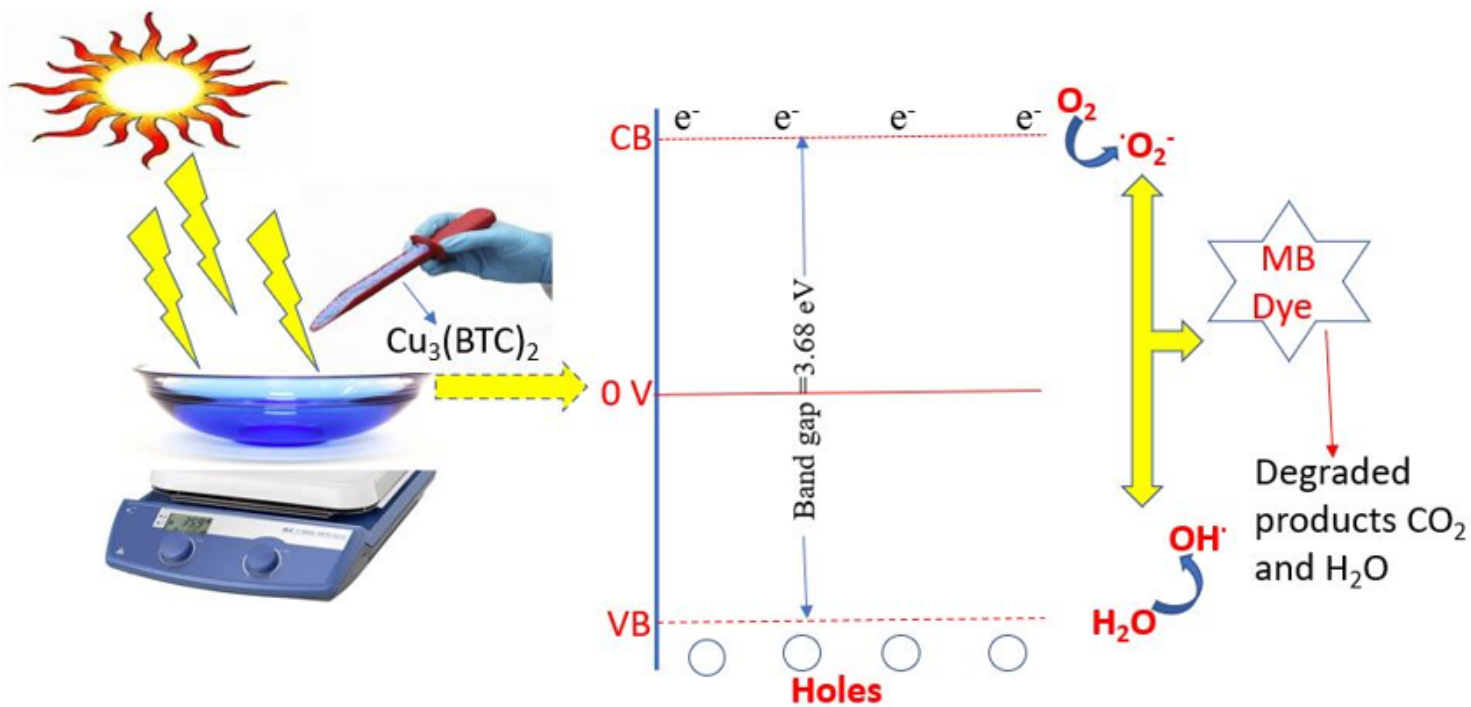


Figure 11

Schematic of photocatalytic degradation mechanism of MB dye solution using $\text{Cu}_3(\text{BTC})_2$ as a photocatalyst under sunlight irradiation.

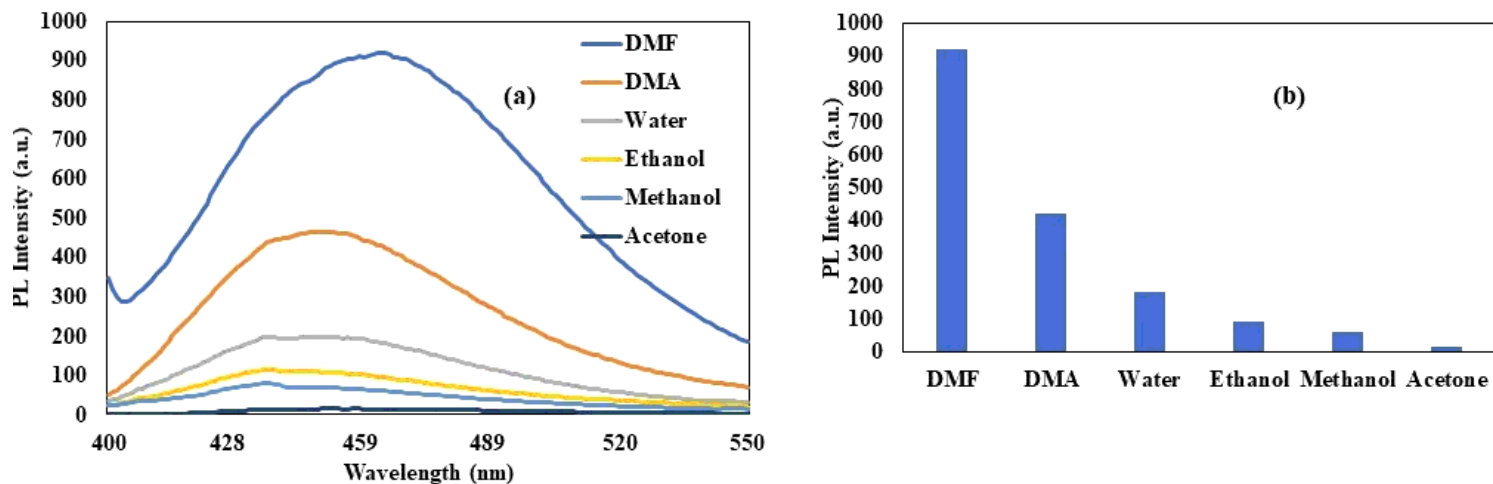


Figure 12

Schematic of photocatalytic degradation mechanism of MB dye solution using Cu₃(BTC)₂ as a photocatalyst under sunlight irradiation.

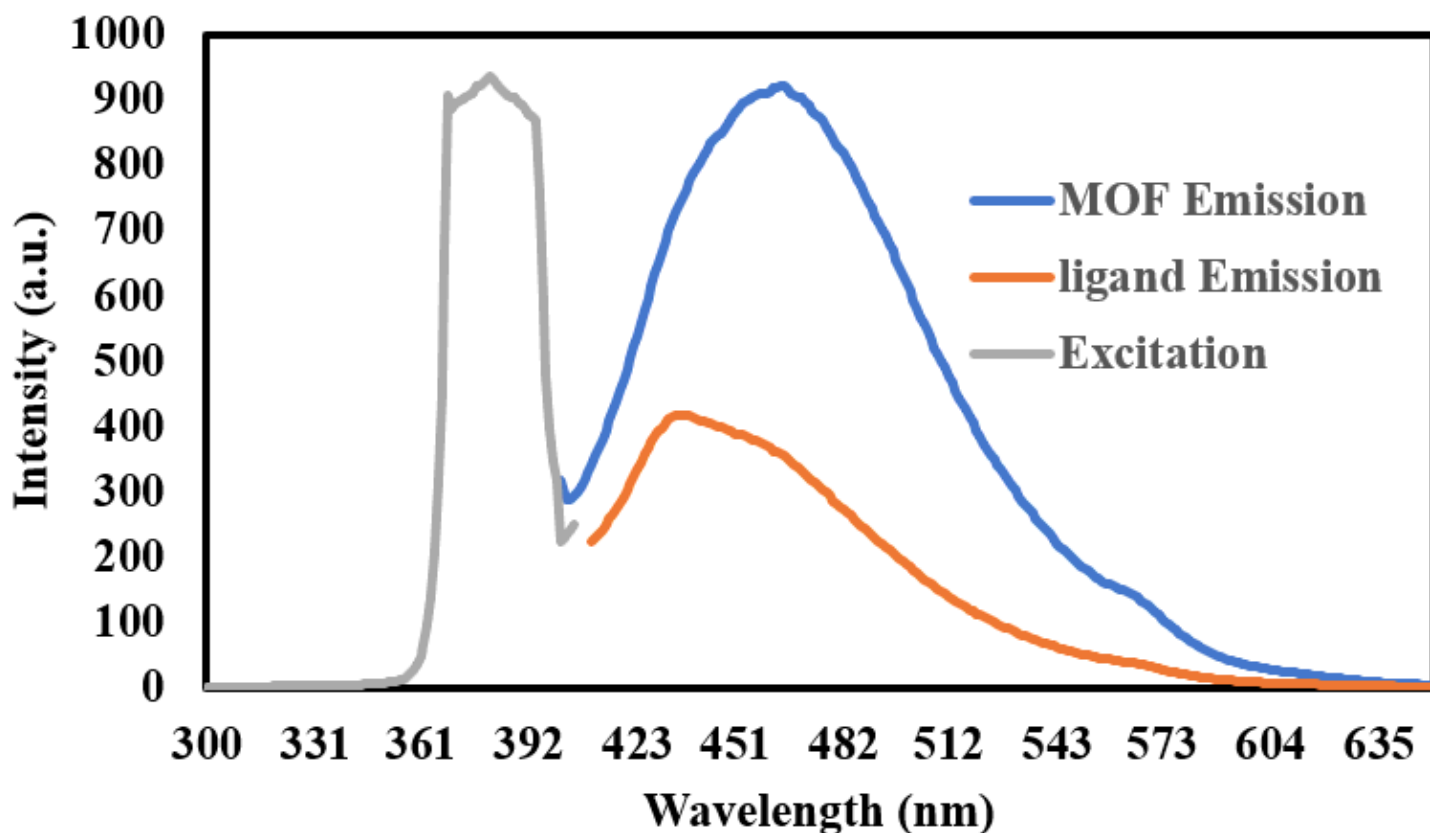


Figure 13

PL spectra of ligand and synthesized MOF, excitation spectra of MOF

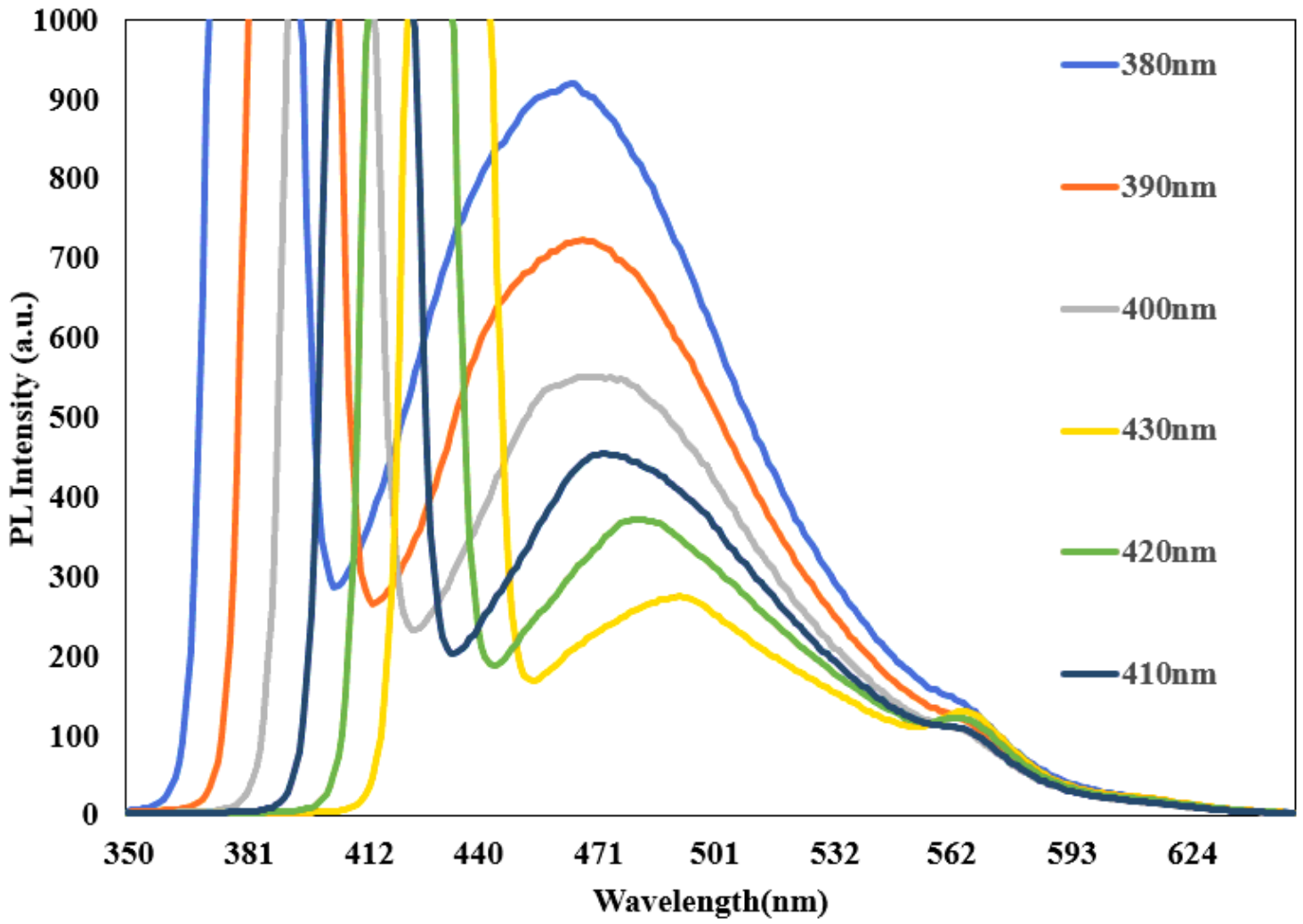


Figure 14

PL spectra of ligand and synthesized MOF, excitation spectra of MOF

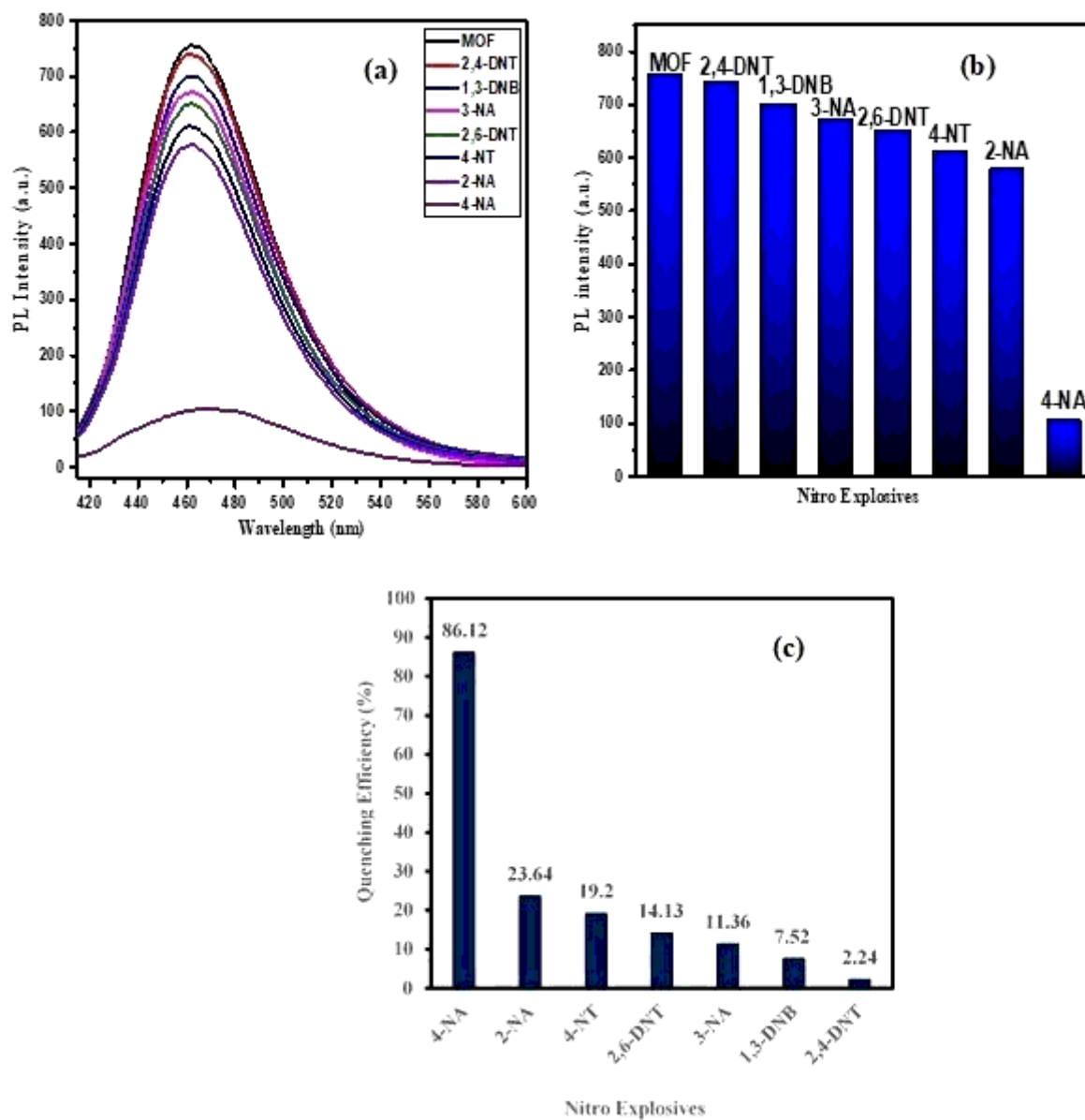


Figure 15

(a): PL spectra of NACs@MOF-199 (100ppb) ($\lambda_{ex} = 380 \text{ nm}$); (b) MOF-199 PL intensity variation as a function of analyte NACs; (c) PL Quenching efficiency of different NACs

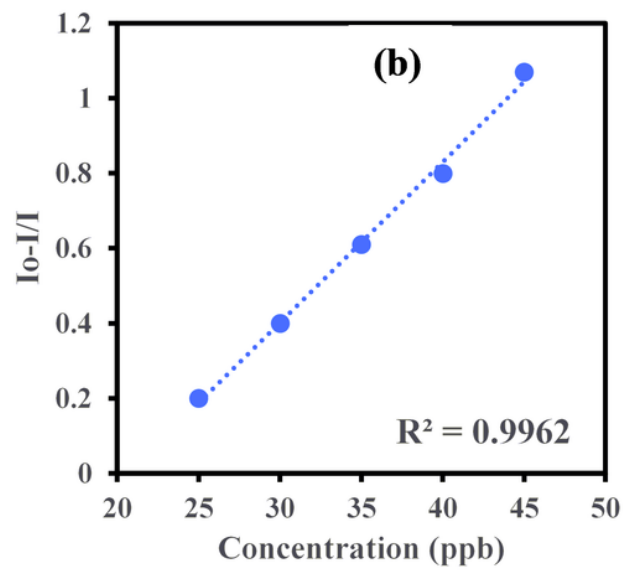
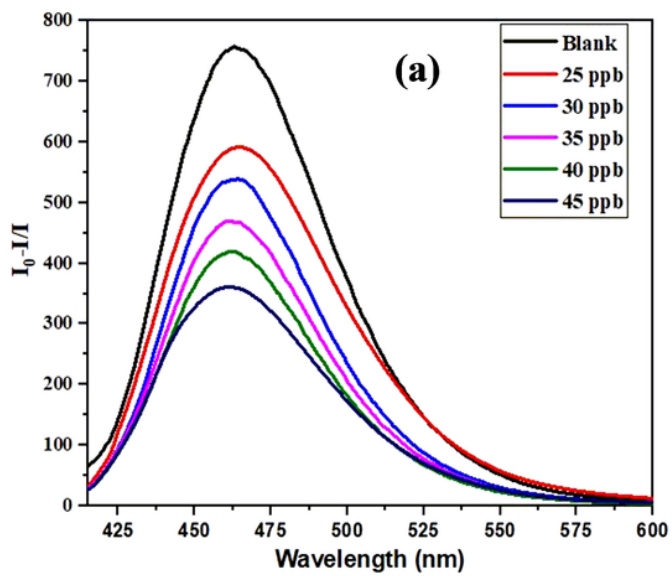


Figure 16

(a): MOF-199 luminescence quenching at different concentration of 4-NA; (b): KSV curve of MOF-199 at different concentrations of 4-NA

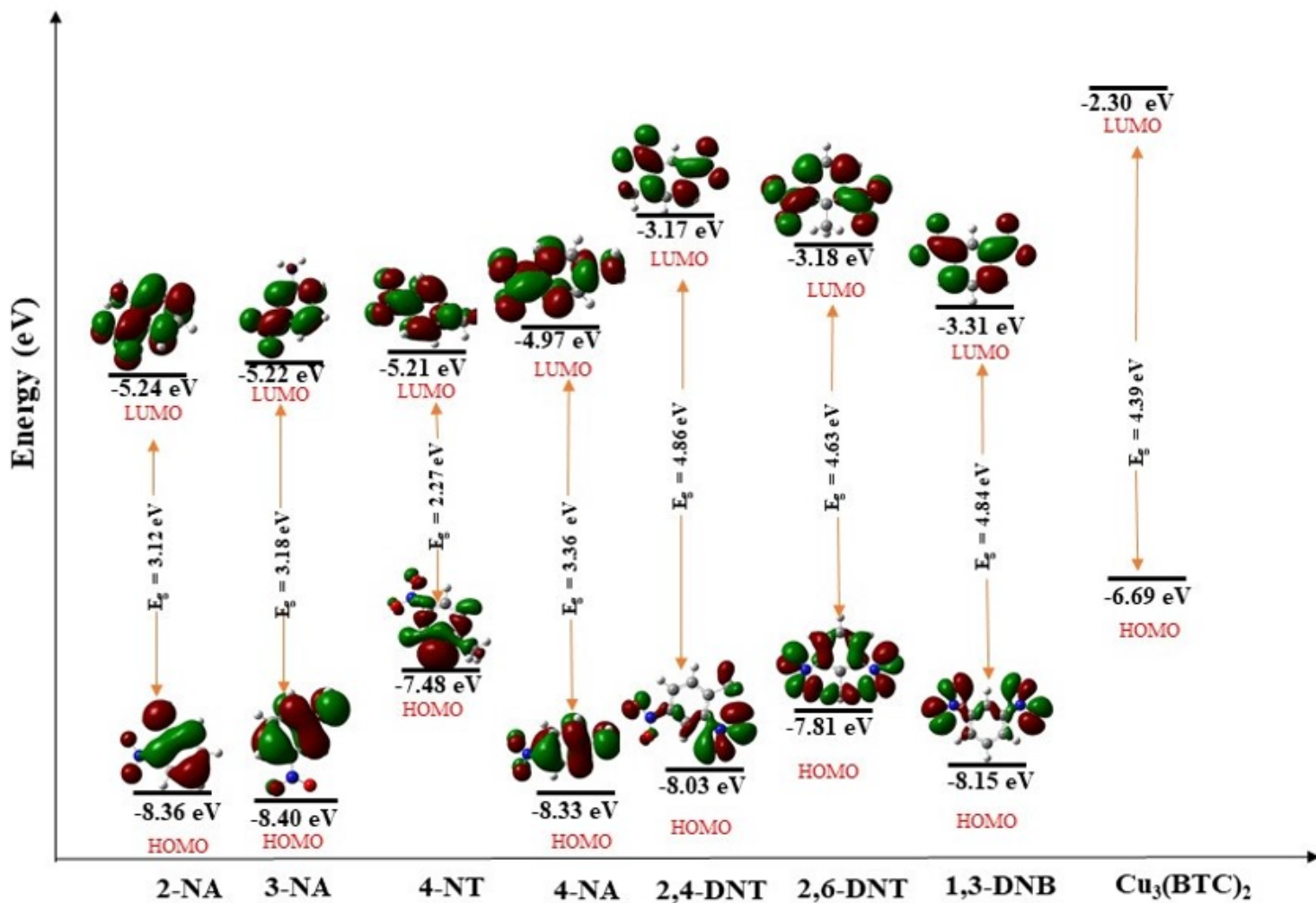


Figure 17

HOMO and LUMO energies of selected nitro aromatic compounds and $\text{Cu}_3(\text{BTC})_2$

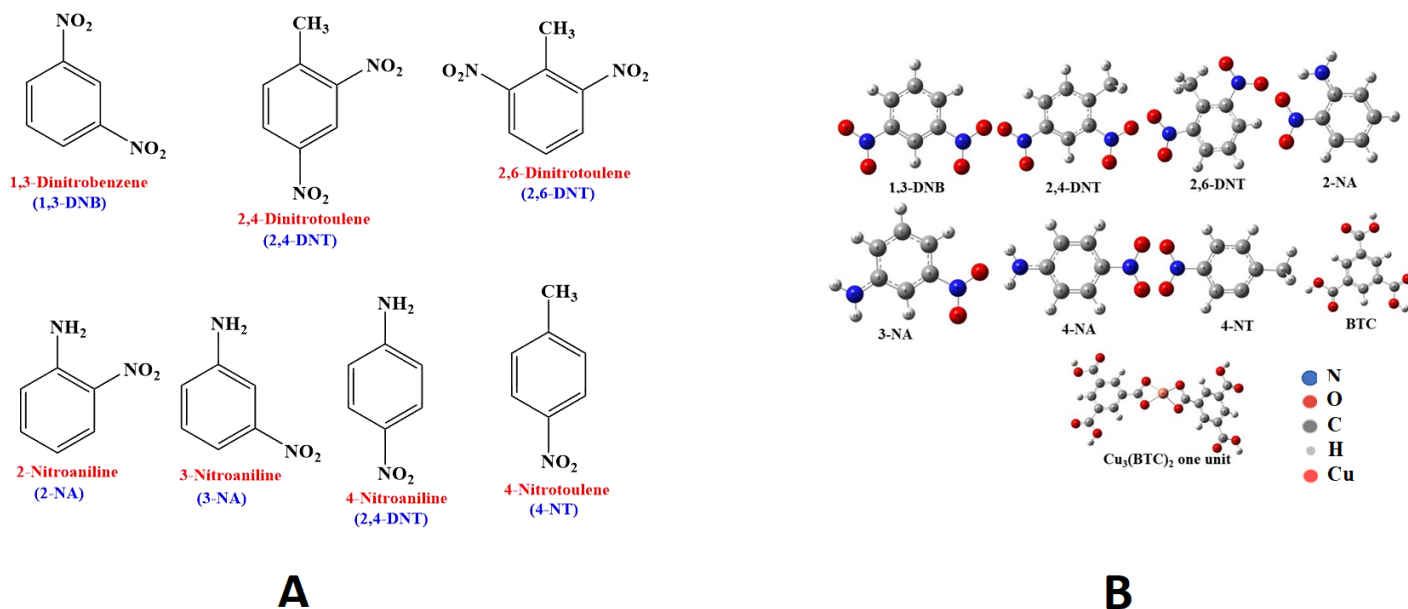


Figure 18

(a) : Structures of different Nitroaromatic Compounds (NACs). (b): Optimized structures of NACs, BTC and one unit of Cu₃(BT

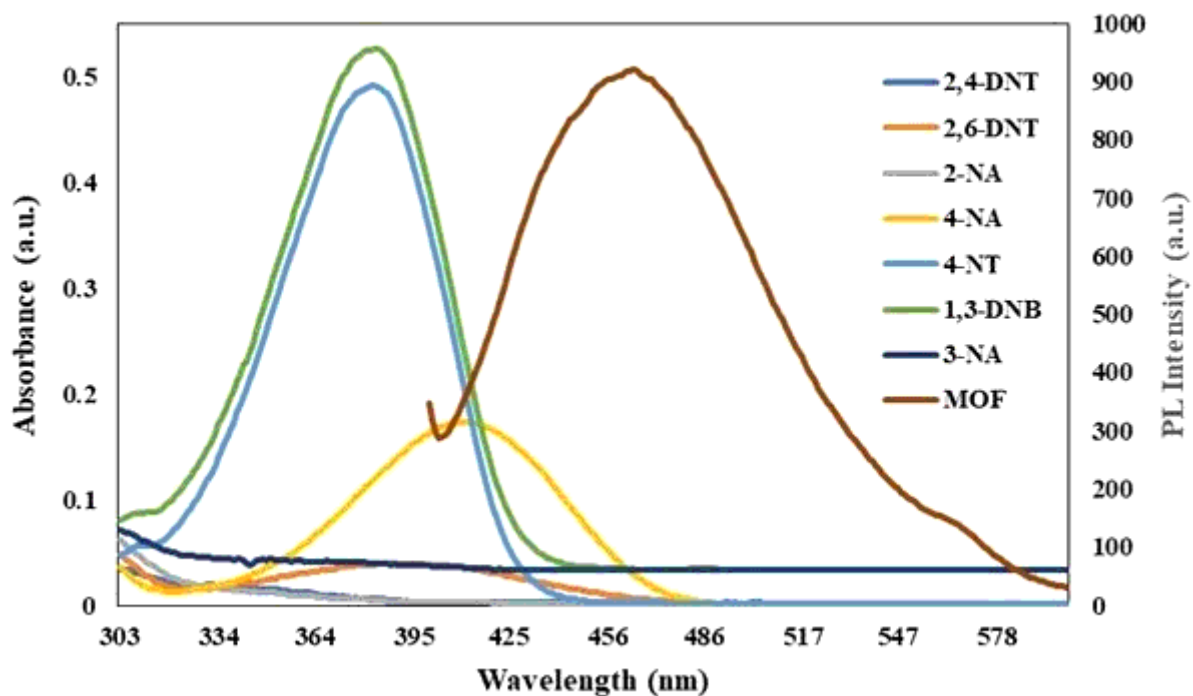


Figure 19

Spectral overlap between the absorption spectra of different NACs and emission spectra of Cu₃(BTC)₂

Supplementary Files

This is a list of supplementary files associated with this preprint. Click to download.

- [Graphicalabstract.jpeg](#)
- [Scheme1.png](#)